Mechanics of Advanced Materials and Structures

ISSN: 1537-6494 (Print) 1537-6532 (Online) Journal homepage: www.tandfonline.com/journals/umcm20

Static analysis of composite and hybrid axisymmetric shells

Carlos A. Mota Soares, José S. Moita, Aurélio L. Araujo, Victor Franco Correia & Cristóvão M. Mota Soares

To cite this article: Carlos A. Mota Soares, José S. Moita, Aurélio L. Araujo, Victor Franco Correia & Cristóvão M. Mota Soares (2025) Static analysis of composite and hybrid axisymmetric shells, Mechanics of Advanced Materials and Structures, 32:24, 6172-6182, DOI: 10.1080/15376494.2025.2537779

To link to this article: https://doi.org/10.1080/15376494.2025.2537779

Published online: 01 Aug 2025.

MECHANICS OF ADVANCED MATERIALS AND STRUCTURES
2025, VOL. 32, NO. 24, 6172–6182
https://doi.org/10.1080/15376494.2025.2537779

Taylor & Francis
Taylor & Francis Group

ORIGINAL ARTICLE

Static analysis of composite and hybrid axisymmetric shells

Carlos A. Mota Soares[a], José S. Moita[b], Aurélio L. Araujo[a], Victor Franco Correia[c], and Cristóvão M. Mota Soares[a]

[a]IDMEC, Instituto Superior Técnico, Universidade de Lisboa, Lisboa, Portugal; [b]IDMEC, Universidade do Algarve, Faro, Portugal; [c]IDMEC, Escola Superior Náutica Infante D. Henrique – ENIDH, Paço de Arcos, Portugal

ABSTRACT

In this work, we present formulations for linear and geometrically nonlinear static analyses of hybrid axisymmetric shell structures. The hybrid structures (F/C/F) are made by layers of composite material (C) sandwiched by two functionally graded material layers (F). The analysis is performed using a finite element model. The numerical solution is obtained by expanding the variables in Fourier series in the circumferential direction and using conical frustum finite elements in the meridional direction. The implemented finite element is a simple conical frustum with two nodal circles. This model uses a small number of discrete layers to model the continuous variation of the mechanical properties through the thickness of the functionally graded material (FGM) layers. It requires a reduced number of finite elements to model the geometry of even complex structures, and the integration procedures uses only one Gauss point. From the combination of those characteristics, the resulting model requires extremely low computation time. A computer program has been developed, and the solutions obtained are discussed and compared with results obtained by alternative models available in the literature. The present plate/shell model provides new insights for future advances to carry out numerical studies involving multi-objective optimization of axisymmetric structures made of advanced materials.

ARTICLE HISTORY
Received 15 May 2025
Accepted 16 July 2025

KEYWORDS
Hybrid axisymmetric shells; static analysis; finite element analysis; numerical results

1. Introduction

Axisymmetric shells are used in a wide range of engineering fields, such as aeronautics and aerospace systems, pressure vessels, cooling towers, and advanced medical equipment, among others. In this work, axisymmetric shell structures are considered, combining composite layered materials with metal-ceramic functionally graded materials. The authors have published several studies involving static linear and geometrically nonlinear analysis, elastoplasticity, free vibrations, and buckling analyses of axisymmetric shell structures applied, separately, to composite laminates and functionally graded materials. In the preparation of those works, the authors have reviewed a large number of works published by other authors, which won't be referenced here. Only a few selected and relevant works are referenced here due to similarity or alternative approaches used and for comparison and validation purposes, in the proper context.

Sheinman and Greif [1] and Sheinman and Weissman [2] presented an analytical and numerical procedures for free and forced vibration of thin-walled shells of revolution, where numerical solution is obtained by expanding the variables in Fourier series in the circumferential direction.

Nath and Kumar [3] used the Chebyshev series solution technique for solving the nonlinear response of cylindrically orthotropic, symmetrically laminated, cross-ply moderately thick plates. Sandeep and Nath [4] carried out the nonlinear axisymmetric static analysis of polar orthotropic, unsymmetrically laminated, cross-ply moderately thick circular plates and shallow spherical shells under uniformly distributed load. Mota Soares et al. [5] in a paper for the optimization of the multi-layered composite axisymmetric shells subjected to arbitrary static loading and free vibrations, use a two-node conical frustum finite element with the displacements expanded in Fourier series in circumferential direction. Pinto Correia et al. [6] using a higher order displacement field, presented a finite element semi-analytical model for laminated axisymmetric shells applied to statics, dynamics and buckling analysis. Santos et al. [7] presented a general semi-analytical finite element model developed for bending, free vibration and buckling analysis of shells of revolution. The 3D elasticity theory is used, and the equations of motion are obtained by expanding the displacement field and load in the Fourier series in terms of the circumferential coordinate.

Flis and Muc [8] studied the axisymmetric deformations of coupled functionally graded spherical shells, using an analytical solution based in complex hypergeometric polynomial series, and showed that for porous FGM shells the influence of the unsymmetric shell wall construction can be described by only one parameter.

CONTACT Aurélio L. Araujo aurelio.araujo@tecnico.ulisboa.pt IDMEC, Instituto Superior Técnico, Universidade de Lisboa, Lisboa, Portugal.

In this article are presented the bending analysis of hybrid axisymmetric shell structures, subjected to axisymmetric and non-axisymmetric loadings, and allowing for different behaviors, linear and geometrically nonlinear deformations. The formulation includes the global response of the hybrid shell structures and the through-thickness stress distribution calculations. The determination of natural frequencies and respective mode shapes was recently published by Moita et al. [9] for axisymmetric shells. Since the present extension is based on the historical developments of Zienckiewics et al. [10] finite element conical frustum, which is a simple finite element with 2 nodal circles, which includes shear deformation effects, introduced through an imposed constraint in the Kirchhoff-Love theory.

The present model is based on separating the variables in a Fourier series in the circumferential direction and conical frustum finite elements in the meridional direction, which have two nodal circles, with 5 or 10 degrees of freedom on each, depending on the analysis to be carried out.

The present extension development reveals to be extremely efficient in the analysis of axisymmetric shells – easy to model the geometry, a low number of total degrees of freedom, very good results, and extremely fast computationally. The results in free vibrations and linear buckling using the present model in Moita et al. [9,11] have shown excellent comparison with alternative solutions.

A particular in-house finite element software for linear and nonlinear finite element analysis has been extended, and the solutions of some illustrative applications have been performed (appendix). The results are presented, discussed and compared with numerical results obtained by alternative models, where available. The present work provides new insights to carry out numerical studies in axisymmetric plates and shells made of advanced materials.

2. Formulation of the hybrid model

For the case of a hybrid FGM-Composite-FGM laminate (F/C/F), as illustrated in Figure 1, it is defined for each composite layer, the principal orthogonal material axes (1,2,3) with direction 1 as the fiber orientation, while an orthogonal layer reference system (s, θ, z'), is applied to the laminate.

For the specific hybrid laminate used in the present work, the total number of layers, N, is $N = 2 \times \mathrm{NF} + \mathrm{NC}$, being NC equal to the number of composite layers (in Figure 1, four composite layers are represented schematically with arbitrary lay-up). The material properties of an FGM structure are assumed to change continuously throughout the thickness, according to the volume fraction of the constituent materials, normally a ceramic and a metal. The continuous variation of the materials mixture is approximated by using the concept of discrete virtual layers throughout the z direction, where each FGM skin is discretized by using an arbitrary number of twenty of those virtual layers (NF = 20).

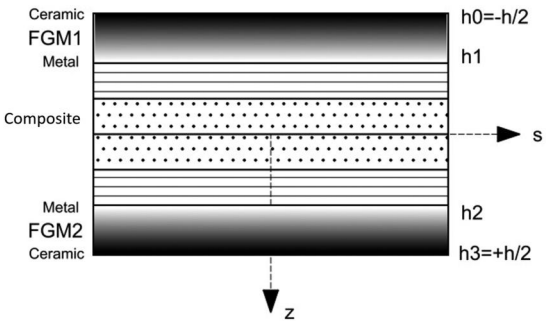

Figure 1. Hybrid plate with laminated composite core and FGM skins.

The volume fraction of the ceramic and metal phases (V_c^k and V_m^k) for each virtual layer are defined as follows:

$$\mathrm{V_c^k} = -\left(\frac{\bar{z} - \mathrm{h_1}}{\mathrm{h_1} - \mathrm{h_0}}\right)^{\mathrm{p}}, z \in [\mathrm{h_0}, \mathrm{h_1}]; \mathrm{V_c^k} = \left(\frac{\bar{z} - \mathrm{h_2}}{\mathrm{h_3} - \mathrm{h_2}}\right)^{\mathrm{p}}, z \in [\mathrm{h_2}, \mathrm{h_3}] \tag{1a}$$

$$\mathrm{V_m^k} = 1.0 - \mathrm{V_c^k} \tag{1b}$$

where $\bar{z}$ is the thickness coordinate of the mid-surface of each layer, and p: a parameter that defines the gradation of material properties through the thickness direction, and $\mathrm{h_0} = -\mathrm{h}/2$, $\mathrm{h_1}$, $\mathrm{h_2}$ and $\mathrm{h_3} = +\mathrm{h}/2$ are the z-coordinates of the interfaces of the layers.

Once the volume fraction $\mathrm{V_c^k}$ and $\mathrm{V_m^k}$ have been defined, the material properties of each layer of an FGM, as for example Young's modulus E and mass density ρ, can be determined by the rule of mixtures:

$$\mathrm{E_k} = \mathrm{V_c^k}\ \mathrm{E_c} + \mathrm{V_m^k}\ \mathrm{E_m}; \rho_\mathrm{k} = \mathrm{V_c^k}\ \rho_\mathrm{c} + \mathrm{V_m^k}\ \rho_\mathrm{m} \tag{2}$$

3. Constitutive matrix and strain–displacement relations

The stress–strain relations are defined based on the stress–strain relations in each layer k, which can be written as follows:

$$\begin{gathered} \{\sigma_\mathrm{k}\} = \left[\overline{\mathrm{Q}}_\mathrm{k}\right]\{\varepsilon_\mathrm{k}\} \\ \sigma_\mathrm{k} = \left\{\sigma_\mathrm{s}^\mathrm{m} \quad \sigma_\theta^\mathrm{m} \quad \sigma_{\mathrm{s}\theta}^\mathrm{m} \quad \sigma_\mathrm{s}^\mathrm{b} \quad \sigma_\theta^\mathrm{b} \quad \sigma_{\mathrm{s}\theta}^\mathrm{b} \quad \sigma_\mathrm{sn}^\mathrm{s} \quad \sigma_{\theta\mathrm{n}}^\mathrm{s}\right\}^\mathrm{T} \\ \varepsilon_\mathrm{k} = \left\{\varepsilon_\mathrm{s}^\mathrm{m} \quad \varepsilon_\theta^\mathrm{m} \quad \gamma_{\mathrm{s}\theta}^\mathrm{m} \quad \varepsilon_\mathrm{s}^\mathrm{b} \quad \varepsilon_\theta^\mathrm{b} \quad \gamma_{\mathrm{s}\theta}^\mathrm{b} \quad \gamma_\mathrm{sn}^\mathrm{s} \quad \gamma_{\theta\mathrm{n}}^\mathrm{s}\right\} \end{gathered} \tag{3}$$

where σ_k and ε_k are the stress and strain vectors, respectively, and $\overline{\mathrm{Q}}_\mathrm{k}$ is the elasticity matrix in the local coordinate system of the laminated composite material being the fiber angle referenced with respect to local direction s.

For axisymmetric shells, the generic local (ℓ) displacement of a point on the middle surface is described by three components u, v and w in the meridional (s), circumferential (θ) and normal ($\mathrm{z}' \equiv \mathrm{n}$) directions, respectively. Introducing transverse shear strains through the imposed constraints $\mathrm{C}(\mathrm{w}, \beta) = \mathrm{dw/ds} - \beta = 0$, (Zienkiewicz et al. [10]), where β are the rotations that can vary independently, the displacement field for a generic point defined by (s, θ, z′) coordinates, using an equivalent single layer model, is given by Moita et al. [9,11] (see, also, Arbind and Reddy [12] and Arbind, Reddy, and Srinivasa [13] for studies that use 1D expansions in the circumferential direction to model tubes and shells of revolution).

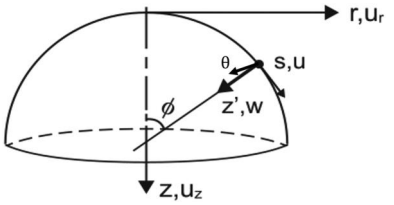

Figure 2. Axisymmetric shell.

$$\begin{Bmatrix} s \\ \theta \\ z' \end{Bmatrix} = \begin{bmatrix} \cos\phi & 0 & \sin\phi \\ 0 & 1 & 0 \\ -\sin\phi & 0 & \cos\phi \end{bmatrix} \begin{Bmatrix} r \\ \theta \\ z \end{Bmatrix};$$

$$\begin{Bmatrix} u_0 \\ v_0 \\ w_0 \\ \beta_s \\ \beta_\theta \end{Bmatrix} = \begin{bmatrix} \cos\phi & 0 & \sin\phi & 0 & 0 \\ 0 & 1 & 0 & 0 & 0 \\ -\sin\phi & 0 & \cos\phi & 0 & 0 \\ 0 & 0 & 0 & 1 & 0 \\ 0 & 0 & 0 & 0 & 1 \end{bmatrix} \begin{Bmatrix} u_{0r} \\ v_0 \\ u_{0z} \\ \beta_s \\ \beta_\theta \end{Bmatrix} \tag{4a}$$

$$\mathbf{d}^{\ell} = \mathbf{T}\ \mathbf{d} \text{ with } \mathbf{d} = \{u_{0r}\ v_0\ \ u_{0z}\ \ \beta_s\ \beta_\theta\} \tag{4b}$$

where $\mathbf{d}^{\ell^T} = \{u_0\ v_0\ \ w_0\ \ \beta_s\ \beta_\theta\}$, being u_0, v_0, w_0 the displacements of a generic point in the middle plane and β_s, β_θ the rotations of the normal to the middle plane, referred to the local axes (s, θ, z′) in Figure 2, and $\mathbf{d}$ is the vector of displacements in global axis, which contains $\overline{d}_i = \{\overline{u}_{0r_i}\ \overline{v}_{0_i}\overline{u}_{0z_i}\overline{\beta}_{s_i}\ \overline{\beta}_{\theta_i}\}$ and $\tilde{d}_i = \{\tilde{u}_{0r_i}\ \tilde{v}_{0_i}\ \ \tilde{u}_{0z_i}\ \ \tilde{\beta}_{s_i}\ \tilde{\beta}_{\theta_i}\}$ that are the symmetric and anti-symmetric parts of the global displacement vector for node i, according to Eq. (7), of next section.

Following the development presented in Moita et al. [9], the constitutive matrix, as well as the strain-displacements relations for the general case of a composite or hybrid laminate with general lay-up, under general load, are respectively:

$$[\hat{D}] = \begin{bmatrix} A_{11} & A_{12} & A_{16} & B_{11} & B_{12} & B_{16} & 0 & 0 \\ A_{21} & A_{22} & A_{26} & B_{21} & B_{22} & B_{26} & 0 & 0 \\ A_{61} & A_{62} & A_{66} & B_{61} & B_{62} & B_{66} & 0 & 0 \\ B_{11} & B_{12} & B_{16} & D_{11} & D_{12} & D_{16} & 0 & 0 \\ B_{21} & B_{22} & B_{26} & D_{12} & D_{22} & D_{26} & 0 & 0 \\ B_{61} & B_{62} & B_{66} & D_{61} & D_{62} & D_{66} & 0 & 0 \\ 0 & 0 & 0 & 0 & 0 & 0 & A_{S_{11}} & A_{S_{12}} \\ 0 & 0 & 0 & 0 & 0 & 0 & A_{S_{21}} & A_{S_{22}} \end{bmatrix} \tag{5}$$

where

$$(\mathbf{A}, \mathbf{B}, \mathbf{D})_k = \overline{\mathbf{Q}}_k \int_{z_{k-1}}^{z_k} (1, z, z^2)\ dz;\ \mathbf{A}_{sk} = \overline{\mathbf{Q}}_k \int_{z_{k-1}}^{z_k} dz \tag{5a}$$

and the strain-displacement relations are:

$$\begin{Bmatrix} \varepsilon_s \\ \varepsilon_\theta \\ \varepsilon_{s\theta} \\ \kappa_s \\ \kappa_\theta \\ \kappa_{s\theta} \\ \gamma_{sz'} \\ \gamma_{\theta z'} \end{Bmatrix} = \begin{Bmatrix} (\partial u_{0r}/\partial s)\cos\phi + (\partial u_{0z}/ds)\sin\phi \\ (u_{0r})/r + (\partial v_0)/r\partial\theta \\ (\partial u_{0r}/r\partial\theta)\cos\phi + (\partial u_{0z}/rd\theta)\sin\phi - (v_0\cos\phi)/r + \partial v_0/\partial s \\ -\partial\beta_s/\partial s \\ -(\beta_s\cos\phi)/r - (\partial\beta_\theta)/r\partial\theta \\ -(\partial\beta_s)/r\partial\theta - (\partial\beta_\theta)/\partial s + (\beta_\theta\cos\phi)/r \\ -(\partial u_{0r}/\partial s)\ \sin\ \phi + (\partial u_{0z}/\partial s)\cos\phi - \beta_s \\ -(\partial u_{0r}/r\partial\theta)\sin\phi + (v_0\sin\phi)/r + (\partial u_{0z}/r\partial\theta)\cos\phi - \beta_\theta \end{Bmatrix} \tag{6}$$

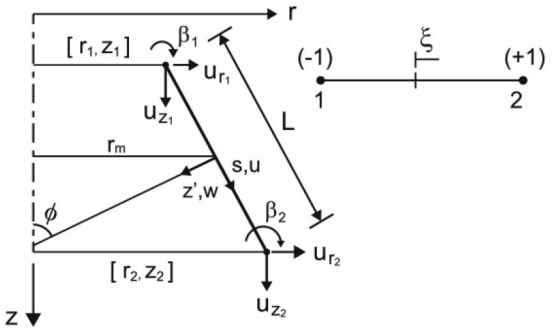

Figure 3. Two-node conical frustum element.

4. Finite element approach and fourier series for axisymmetric structures

4.1. Static linear analysis for general loads

The global displacements and rotations are expanded in Fourier series, for circumferentional direction (θ) (Sheinman and Greif [1]).

$$u_{0r} = \sum_{n=0}^{nh}(\overline{u}_{0r_n}\cos n\theta + \tilde{u}_{0r_n}\sin n\theta), v_0 = \sum_{n=0}^{nh}(\overline{v}_{0_n}\sin n\theta + \tilde{v}_{0_n}\cos n\theta)$$
$$u_{0z} = \sum_{n=0}^{nh}(\overline{u}_{0z_n}\cos n\theta + \tilde{u}_{0z_n}\sin n\theta), \beta_s = \sum_{n=0}^{nh}(\overline{\beta}_{sn}\cos n\theta + \tilde{\beta}_{sn}\sin n\theta)$$
$$\beta_\theta = \sum_{n=0}^{nh}(\overline{\beta}_{\theta n}\sin n\theta + \tilde{\beta}_{\theta n}\cos n\theta) \tag{7}$$

where $\overline{d}_{in} = \{\overline{u}_{0r_i}\ \overline{v}_{0_i}\overline{u}_{0z_i}\overline{\beta}_{s_i}\ \overline{\beta}_{\theta_i}\}_n$ and $\tilde{d}_{in} = \{\tilde{u}_{0r_i}\ \tilde{v}_{0_i}\ \tilde{u}_{0z_i}\tilde{\beta}_{s_i}\ \tilde{\beta}_{\theta_i}\}_n$ are the element symmetric and antisymmetric parts of the displacements and rotations amplitudes at the nodal points for the n^{th} harmonic.

The displacements and rotations at any point of reference surface are approximated in the meridional direction (s) through the shape functions N_i of a conical frustum – straight finite element, shown in Figure 3, with 2 nodal circles and 5 or 10 degrees of freedom per node. In Figure 3, the degrees of freedom v and β_θ are not represented.

The simplest interpolation functions are $N_i = (1 + \xi_i\xi)/2$ with $\xi = \pm 1$ and $A^e = 2\ \pi\ r_m\ ds = \pi\ r_m\ L\ d\xi = 2\ \pi\ r_m\ L$. For example, the symmetric displacement vector and the element linear strains in the global coordinate system can be written in the form:

$$\begin{Bmatrix} \overline{u}_{0_r} \\ \overline{v}_0 \\ \overline{u}_{0_z} \\ \overline{\beta}_s \\ \overline{\beta}_\theta \end{Bmatrix}_n = \sum_{i=1}^{2} \begin{bmatrix} N_i\cos n\theta & 0 & 0 & 0 & 0 \\ 0 & N_i\sin n\theta & 0 & 0 & 0 \\ 0 & 0 & N_i\cos n\theta & 0 & 0 \\ 0 & 0 & 0 & N_i\cos n\theta & 0 \\ 0 & 0 & 0 & 0 & N_i\sin n\theta \end{bmatrix} \begin{Bmatrix} \overline{u}_{0ri} \\ \overline{v}_{0i} \\ \overline{u}_{0zi} \\ \overline{\beta}_{si} \\ \overline{\beta}_{\theta i} \end{Bmatrix} \tag{8-a}$$

$$\bar{\mathbf{d}}_n = \left[\bar{\theta}_n^B\right]\mathbf{N}_i d_{in};$$
$$\bar{\varepsilon}_n = \sum_{i=1}^{2}\left[\bar{\theta}_n^B\right]\ \bar{\mathbf{B}}_{i_n}\ \bar{\mathbf{d}}_{i_n} = \left[\bar{\theta}_n^B\right]\bar{\mathbf{B}}_n\ \bar{\mathbf{d}}_n \tag{8-b}$$

Applying the Virtual Work Principle, the linear strain energy, given by $U = \int_A \delta\ \{\boldsymbol{\varepsilon}\}^T[\hat{\mathbf{D}}]\{\boldsymbol{\varepsilon}\}dA$, becomes:

$$U = \int_A \delta\ \overline{d}^T\overline{B}^T\left[\overline{\theta}^B\right]^T\hat{D}\ \left[\overline{\theta}^B\right]\overline{B}\ \overline{d}\ dA\ + \int_A \delta\ \overline{d}^T\overline{B}^T\left[\overline{\theta}^B\right]^T\hat{D}\ \left[\tilde{\theta}^B\right]\tilde{B}\ \tilde{d}\ d + \int_A \delta\ \tilde{d}^T\tilde{B}^T\ [\tilde{\theta}]^T\hat{D}\ \left[\overline{\theta}^B\right]\overline{B}\ \overline{d}\ dA + \int_A \delta\ \tilde{d}^T\tilde{B}^T\left[\tilde{\theta}^B\right]^T\hat{D}\ \left[\tilde{\theta}^B\right]\tilde{B}\ \tilde{d}\ dA \tag{9a}$$

and following the development presented in Moita et al [9,11], where the terms of matrices $[\overline{\theta}_n]$, $[\tilde{\theta}_n]$, $[\overline{B}_n]$ $[\tilde{B}_n]$ can be found, the element stiffness matrix can be obtained as:

$$[\mathbf{K}_n] = \begin{bmatrix} \overline{B}_1{}^T[\overline{D}]\ \overline{B}_1 & \overline{B}_1{}^T[\hat{D}]\ \tilde{B}_1 & \overline{B}_1{}^T[\overline{D}]\ \overline{B}_2 & \overline{B}_1{}^T[\hat{D}]\ \tilde{B}_2 \\ \tilde{B}_1{}^T[\breve{D}]\ \overline{B}_1 & \tilde{B}_1{}^T[\tilde{D}]\ \tilde{B}_1 & \tilde{B}_1{}^T[\breve{D}]\ \overline{B}_2 & \tilde{B}_1{}^T[\hat{D}]\ \tilde{B}_2 \\ \overline{B}_2{}^T[\overline{D}]\ \overline{B}_1 & \overline{B}_2{}^T[\hat{D}]\ \tilde{B}_1 & \overline{B}_2{}^T[\overline{D}]\ \overline{B}_2 & \overline{B}_2{}^T[\hat{D}]\ \tilde{B}_2 \\ \tilde{B}_2{}^T[\breve{D}]\ \overline{B}_1 & \tilde{B}_2{}^T[\tilde{D}]\ \tilde{B}_1 & \tilde{B}_2{}^T[\breve{D}]\ \overline{B}_2 & \tilde{B}_2{}^T[\tilde{D}]\ \tilde{B}_2 \end{bmatrix} \tag{9b}$$

with

$$[\overline{\mathbf{D}}] = \left[\overline{\boldsymbol{\theta}}_n^B\right]^T[\hat{\mathbf{D}}]\left[\overline{\boldsymbol{\theta}}_n^B\right]; [\tilde{\mathbf{D}}] = \left[\tilde{\boldsymbol{\theta}}_n^B\right]^T[\hat{\mathbf{D}}]\left[\tilde{\boldsymbol{\theta}}_n^B\right] \tag{9c}$$

$$\left[\hat{\mathbf{D}}\right] = \left[\overline{\boldsymbol{\theta}}_n^B\right]^T[\hat{\mathbf{D}}]\left[\tilde{\boldsymbol{\theta}}_n^B\right]; [\breve{\mathbf{D}}] = \left[\tilde{\boldsymbol{\theta}}_n^B\right]^T[\hat{\mathbf{D}}]\left[\overline{\boldsymbol{\theta}}_n^B\right]$$

$$\left[\overline{\theta}^B\right] = \begin{bmatrix} C & 0 & 0 & 0 & 0 & 0 & 0 & 0 \\ 0 & C & 0 & 0 & 0 & 0 & 0 & 0 \\ 0 & 0 & S & 0 & 0 & 0 & 0 & 0 \\ 0 & 0 & 0 & C & 0 & 0 & 0 & 0 \\ 0 & 0 & 0 & 0 & C & 0 & 0 & 0 \\ 0 & 0 & 0 & 0 & 0 & S & 0 & 0 \\ 0 & 0 & 0 & 0 & 0 & 0 & C & 0 \\ 0 & 0 & 0 & 0 & 0 & 0 & 0 & S \end{bmatrix}; \tag{9d}$$

$$\left[\tilde{\theta}^B\right] = \begin{bmatrix} S & 0 & 0 & 0 & 0 & 0 & 0 & 0 \\ 0 & S & 0 & 0 & 0 & 0 & 0 & 0 \\ 0 & 0 & C & 0 & 0 & 0 & 0 & 0 \\ 0 & 0 & 0 & S & 0 & 0 & 0 & 0 \\ 0 & 0 & 0 & 0 & S & 0 & 0 & 0 \\ 0 & 0 & 0 & 0 & 0 & C & 0 & 0 \\ 0 & 0 & 0 & 0 & 0 & 0 & S & 0 \\ 0 & 0 & 0 & 0 & 0 & 0 & 0 & C \end{bmatrix}$$

with $S = \sin(n\theta)$ and $C = \cos(n\theta)$.

Using of the orthogonality properties of trigonometric functions, it can be written:

$$[\overline{D}] = \begin{bmatrix} A_{11}c^2 & A_{12}c^2 & 0 & B_{11}c^2 & B_{12}c^2 & 0 & 0 & 0 \\ A_{21}c^2 & A_{22}c^2 & 0 & B_{21}c^2 & B_{22}c^2 & 0 & 0 & 0 \\ 0 & 0 & A_{66}s^2 & 0 & 0 & B_{66}s^2 & 0 & 0 \\ B_{11}c^2 & B_{12}c^2 & 0 & D_{11}c^2 & D_{12}c^2 & D_{16} & 0 & 0 \\ B_{21}c^2 & B_{22}c^2 & 0 & D_{22}c^2 & D_{22}c^2 & D_{26} & 0 & 0 \\ 0 & 0 & B_{66}s^2 & 0 & 0 & D_{66}s^2 & 0 & 0 \\ 0 & 0 & 0 & 0 & 0 & 0 & A_{s11}c^2 & 0 \\ 0 & 0 & 0 & 0 & 0 & 0 & 0 & A_{s22}s^2 \end{bmatrix} \tag{10a}$$

$$[\tilde{D}] = \begin{bmatrix} A_{11}s^2 & A_{12}s^2 & 0 & B_{11}s^2 & B_{12}s^2 & 0 & 0 & 0 \\ A_{11}s^2 & A_{22}s^2 & 0 & B_{21}s^2 & B_{22}s^2 & 0 & 0 & 0 \\ 0 & 0 & A_{66}c^2 & 0 & 0 & B_{66}c^2 & 0 & 0 \\ B_{11}s^2 & B_{12}s^2 & 0 & D_{11}s^2 & D_{12}s^2 & 0 & 0 & 0 \\ B_{21}s^2 & B_{22}s^2 & 0 & D_{22}s^2 & D_{22}s^2 & 0 & 0 & 0 \\ 0 & 0 & B_{66}c^2 & 0 & 0 & D_{66}c^2 & 0 & 0 \\ 0 & 0 & 0 & 0 & 0 & 0 & A_{s22}s^2 & 0 \\ 0 & 0 & 0 & 0 & 0 & 0 & 0 & A_{s22}c^2 \end{bmatrix} \tag{10b}$$

$$[\hat{D}] = \begin{bmatrix} 0 & 0 & A_{16}c^2 & 0 & 0 & B_{16}c^2 & 0 & 0 \\ 0 & 0 & A_{26}c^2 & 0 & 0 & B_{16}c^2 & 0 & 0 \\ A_{61}s^2 & A_{62}s^2 & 0 & B_{61}s^2 & B_{62}s^2 & 0 & 0 & 0 \\ 0 & 0 & B_{16}c^2 & 0 & 0 & D_{16}c^2 & 0 & 0 \\ 0 & 0 & B_{26}c^2 & 0 & 0 & D_{26}c^2 & 0 & 0 \\ B_{61}s^2 & B_{62}s^2 & 0 & D_{61}s^2 & D_{62}s^2 & 0 & 0 & 0 \\ 0 & 0 & 0 & 0 & 0 & 0 & 0 & A_{s12}s^2 \\ 0 & 0 & 0 & 0 & 0 & 0 & A_{s12}c^2 & 0 \end{bmatrix} \tag{10c}$$

$$[\breve{D}] = \begin{bmatrix} 0 & 0 & A_{16}s^2 & 0 & 0 & A_{16}s^2 & 0 & 0 \\ 0 & 0 & A_{26}s^2 & 0 & 0 & B_{16}s^2 & 0 & 0 \\ A_{61}c^2 & A_{62}c^2 & 0 & B_{61}c^2 & B_{62}c^2 & 0 & 0 & 0 \\ 0 & 0 & B_{16}s^2 & 0 & 0 & D_{16}s^2 & 0 & 0 \\ 0 & 0 & B_{26}s^2 & 0 & 0 & D_{26}s^2 & 0 & 0 \\ B_{61}c^2 & B_{62}c^2 & 0 & D_{61}c^2 & D_{62}c^2 & 0 & 0 & 0 \\ 0 & 0 & 0 & 0 & 0 & 0 & 0 & A_{12}c^2 \\ 0 & 0 & 0 & 0 & 0 & 0 & A_{21}s^2 & 0 \end{bmatrix} \tag{10d}$$

For the case of composite or hybrid laminates with lay-ups yielding $A_{i6} = 0, B_{i6} = 0, D_{i6} = 0$ with $i = 1,2$, in the constitutive matrix $[\hat{D}]$ (Eq. (5)), there is no coupling between symmetric and antisymmetric parts of displacements. For lay-ups yielding $A_{i6} \neq 0, B_{i6} \neq 0, D_{i6} \neq 0$, coupling exists, and acts on the element stiffness matrix of each harmonic through the constitutive matrix.

However, in general, it is difficult to predict, even for the particular cases mentioned above, if there is coupling or not. For the case of axisymmetric shells under axisymmetric load, and the composite laminated with fiber orientations not equal to 0 or 90 degrees, the symmetry to the middle plan could be not enough. But if the lay-up is symmetric and balanced, then no coupling exists.

4.2. Interior pressure load

The pressure vector is expanded in Fourier series, for circumferentional direction θ, as

$$p = \sum_{n=0}^{NH}\left(\overline{p}_n \cos\ n\theta + \tilde{p}_n \sin\ n\theta\right) \tag{11}$$

and following the development presented in Moita et al. [11], it becomes:

$$\overline{F}_n^{ext} = \int_0^{2\pi}\left(\sum_{i=1}^{2}\begin{bmatrix} N_i & 0 & 0 \\ 0 & N_i & 0 \\ 0 & 0 & N_i \end{bmatrix}\begin{Bmatrix} \overline{p}_{r_i}C^2 \\ \overline{p}_{v_i}S^2 \\ \overline{p}_{z_i}C^2 \end{Bmatrix}\right) r^e\ L^e\ d\theta \tag{12a}$$

$$\tilde{F}_n^{ext} = \int_0^{2\pi} \left(\sum_{i=1}^{2} \begin{bmatrix} N_i & 0 & 0 \\ 0 & N_i & 0 \\ 0 & 0 & N_i \end{bmatrix} \begin{Bmatrix} \tilde{p}_{r_i} S^2 \\ \tilde{p}_{v_i} C^2 \\ \tilde{p}_{z_i} S^2 \end{Bmatrix} \right) r^e \; L^e \; d\theta \tag{12b}$$

After assembling all the elements, the static problem takes the following form:

$$[K_n]\{q_n\} = \{F_n^{ext}\} \tag{13}$$

$$\{q\} = \{q_0\} + \{q_1\} + \ldots + \{q_n\} \tag{14}$$

In the present work, static analysis of axisymmetric shells is performed. The case of a horizontal cylinder full of water, for example, cannot be modeled with zero harmonics. To model the nonsymmetrical load, we need to consider the harmonic $n=0$ and the harmonic $n=1$. In this case, the radial deformation is obtained as follows:

$$\begin{array}{c} [K_0]\{q_0\} = \{F_0^{ext}\} \\ [K_1]\{q_1\} = \{F_1^{ext}\} \\ \{q\} = \{q_0\} + \{q_1\} \end{array} \tag{15}$$

4.3. Static geometrically nonlinear analysis for axisymmetric loads

For shells of revolution with uniform circumferential properties, the thickness with lay-up symmetric and balanced, the response to axisymmetric loading, is axisymmetric. The governing equations are obtained by setting the Fourier harmonic $n=0$, i.e. all the antisymmetric terms vanish in the displacement vector, resultant forces and moments, and external load vector. It means that from Eq. (5), the terms $A_{i6}, B_{i6}, D_{i6},$ with i=1,2, in matrix $[\hat{D}_0]$ are equal to zero and also zero in matrix $[\overline{D}_0]$. All other terms in the stiffness matrix (Eq. (9a)) containing $[\tilde{D}_0], [\hat{D}_0]$and $[\check{D}_0]$, are zero. Thus, there is no coupling and the antisymmetric terms vanish. Thus, we have the following global displacement vector $\overline{\mathbf{d}}_i = \{\overline{u}_{0r_i} \; \overline{v}_{0_i} \overline{u}_{0z_i} \overline{\beta}_{s_i} \; \overline{\beta}_{\theta_i}\}$. The strain-displacement vector is that given by Eq. (6) and the constitutive matrix is:

$$[\overline{D}] = \left[\overline{\theta}_n^B\right]^T [\hat{D}] \left[\overline{\theta}_n^B\right]$$

$$= \begin{bmatrix} A_{11}C^2 & A_{12}C^2 & 0 & B_{11}C^2 & B_{12}C^2 & 0 & 0 & 0 \\ A_{21}C^2 & A_{12}C^2 & 0 & B_{21}C^2 & B_{22}C^2 & 0 & 0 & 0 \\ 0 & 0 & 0 & 0 & 0 & 0 & 0 & 0 \\ B_{11}C^2 & B_{12}C^2 & 0 & D_{11}C^2 & D_{12}C^2 & 0 & 0 & 0 \\ B_{21}C^2 & B_{22}C^2 & 0 & D_{21}C^2 & D_{22}C^2 & 0 & 0 & 0 \\ 0 & 0 & 0 & 0 & 0 & 0 & 0 & 0 \\ 0 & 0 & 0 & 0 & 0 & 0 & A_{S_{11}}C^2 & 0 \\ 0 & 0 & 0 & 0 & 0 & 0 & 0 & 0 \end{bmatrix} \tag{16}$$

and finally, the linear stiffness matrix can be represented as:

$$[K_0] = \begin{bmatrix} \overline{B}_1{}^T \overline{D} \; \overline{B}_1 & \overline{B}_1{}^T \overline{D} \; \overline{B}_2 \\ \overline{B}_2{}^T \overline{D} \; \overline{B}_1 & \overline{B}_2{}^T \overline{D} \; \overline{B}_2 \end{bmatrix} \tag{17}$$

To account for nonlinear response, nonlinear strains $\boldsymbol{\varepsilon}^{NL} = \frac{1}{2}\,\mathbf{d}^T\,\mathbf{G}^T\mathbf{G}\,\mathbf{d}$ have to be considered in the Virtual Work Principle, that is $U_\sigma \int_A \delta\, \varepsilon^{NL^T} \hat{\boldsymbol{\sigma}}\, dA$. Following the development of Moita et al. [11], for the particular case of axisymmetric composite or hybrid structures, under axisymmetric loading (i.e. $n=0$), and symmetric material to the middle surface of thickness, results the matrices for $\overline{G}$ and $\overline{\sigma}$.

The nonlinear strain vector is then given by:

$$\varepsilon^{NL} = \frac{1}{2} \begin{Bmatrix} (du/ds)^2 + (dv/ds)^2 + (dw/ds)^2 \\ (du/rd\theta)^2 + (dv/rd\theta)^2 + (dw/rd\theta)^2 \\ (du/ds)(du/rd\theta) + (dv/ds)(dv/rd\theta) + (dw/ds)(dw/rd\theta) \end{Bmatrix} \tag{18a}$$

$$\overline{\varepsilon}_n^{NL} = \sum_{i=1}^{2} (\overline{d}_{i_n}^T \overline{G}_{i_n}^T \left[\overline{\theta}_n^G\right]^T \left[\overline{\theta}_n^G\right] \overline{G}_{i_n} \overline{d}_{i_n}) \tag{18b}$$

with

$$[\overline{\theta}_G] = \begin{bmatrix} C & 0 & 0 & 0 & 0 & 0 \\ 0 & S & 0 & 0 & 0 & 0 \\ 0 & 0 & S & 0 & 0 & 0 \\ 0 & 0 & 0 & C & 0 & 0 \\ 0 & 0 & 0 & 0 & C & 0 \\ 0 & 0 & 0 & 0 & 0 & S \end{bmatrix};$$

$$\overline{G}_{i_n} = \begin{bmatrix} \frac{\partial N_i}{\partial s}\cos\phi & 0 & \frac{\partial N_i}{\partial s}\sin\phi & 0 & 0 \\ -n\frac{N_i}{r}\cos\phi & 0 & -n\frac{N_i}{r}\sin\phi & 0 & 0 \\ 0 & \frac{\partial N_i}{\partial s} & 0 & 0 & 0 \\ 0 & n\frac{N_i}{r} & 0 & 0 & 0 \\ -\frac{\partial N_i}{\partial s}\sin\phi & 0 & \frac{\partial N_i}{\partial s}\cos\phi & 0 & 0 \\ n\frac{N_i}{r}\sin\phi & 0 & -n\frac{N_i}{r}\cos\phi & 0 & 0 \end{bmatrix} \tag{19}$$

and

$$\left[\overline{\theta}_{G_n}\right]^T \hat{\sigma} \; \left[\overline{\theta}_{G_n}\right] = [\overline{\sigma}_n];$$

$$\hat{\sigma} = \begin{bmatrix} N_S & N_{S\theta} & 0 & 0 & 0 & 0 \\ N_{S\theta} & N_\theta & 0 & 0 & 0 & 0 \\ 0 & 0 & N_S & N_{S\theta} & 0 & 0 \\ 0 & 0 & N_{S\theta} & N_\theta & 0 & 0 \\ 0 & 0 & 0 & 0 & N_S & N_{S\theta} \\ 0 & 0 & 0 & 0 & N_{S\theta} & N_\theta \end{bmatrix} \tag{20}$$

$$U_{\sigma_n} = \int_A \delta\, \overline{d}^T \overline{G}^T [\overline{\sigma}_n] \overline{G}\; \overline{d}\; dA \tag{21}$$

where $\overline{\sigma}$ is given in Moita et al (11), resulting for the geometric stiffness matrix

$$[K_{G_n}] = \begin{bmatrix} \bar{G}_1{}^T \bar{\sigma} \bar{G}_1 & 0 & \bar{G}_1{}^T \bar{\sigma} \bar{G}_2 & 0 \\ 0 & \tilde{G}_1{}^T \tilde{\sigma} \tilde{G}_1 & 0 & \tilde{G}_1{}^T \tilde{\sigma} \tilde{G}_2 \\ \bar{G}_2{}^T \bar{\sigma} \bar{G}_1 & 0 & \bar{G}_2{}^T \bar{\sigma} \bar{G}_2 & 0 \\ 0 & \tilde{G}_2{}^T \tilde{\sigma} \tilde{G}_1 & 0 & \tilde{G}_2{}^T \tilde{\sigma} \tilde{G}_2 \end{bmatrix} \tag{22}$$

For the referred cases of linear stiffness matrix, and being $n=0$, the antisymmetric terms vanish in the displacement vector, and the nonlinear strain energy in Virtual Work Principle is given by:

$$U_{\sigma_0} = \int_A \delta \left\{ \overline{d}_{1_0} \quad \overline{d}_{2_0} \right\} \begin{Bmatrix} \overline{G}_{1_0} \\ \overline{G}_{20} \end{Bmatrix} [\overline{\sigma}_0] \left\{ \overline{G}_{1_0} \quad \overline{G}_{2_0} \right\} \begin{Bmatrix} \overline{d}_{1_0} \\ \overline{d}_{2_0} \end{Bmatrix} dA \tag{23}$$

resulting, finally, for the geometric stiffness matrix or stiffness matrix of initial stresses:

$$[K_{G_0}] = \begin{bmatrix} \overline{G}_{1_0}{}^T \overline{\sigma}_0 \, \overline{G}_{1_0} & \overline{G}_{1_0}{}^T \overline{\sigma}_0 \, \overline{G}_{2_0} \\ \overline{G}_{2_0}{}^T \overline{\sigma}_0 \, \overline{G}_{1_0} & \overline{G}_{2_0}{}^T \overline{\sigma}_0 \, \overline{G}_{2_0} \end{bmatrix}_n \tag{24}$$

The virtual work principle is used in conjugation with an updated Lagrangian formulation. The system of equilibrium equations is given by:

$$^{t+\Delta t}_{t+\Delta t}(K_0 + K_{G_0})^{(i-1)} \, \Delta q^{(i)} = {}^{t+\Delta t}F_{ext} - {}^{t+\Delta t}_{t+\Delta t}F^{(i-1)}_{int} \tag{25}$$

with

$$\overline{F}_{int} = \int_{A^e} \overline{B}^T \, \overline{\sigma} \, dA^e. \tag{26}$$

Using the Newton-Raphson incremental-iterative method, the incremental equilibrium path is obtained.

It should be noted that only for vibrations and buckling analysis, and for unsymmetric static loading, like a hydrostatic pressure, for example, it is necessary to use a number of harmonics greater than zero.

5. Applications

5.1. Nonlinear analysis of circular composite plate under uniform pressure load

A composite circular plate, subjected to a uniform pressure load, as represented in Figure 4, is analyzed. The dimensions of the plate are radius $R=0.4$ and thickness $h=0.01$ m, and the mechanical properties of graphite-epoxy are given by: $E_2/E_1 = 40$, $(G_{12} = G_{13})/E_1 = 0.5$, $\nu_{12} = 0.25$. Three cases of lamination lay-ups are considered: single layer [0°], three layers [0°/90°/0°], and nine layers [0°/90°/0°/90°/0°/90°/0°/90°/0°] where, in this case, 0° is the circumferential direction and 90° is the radial direction. Defining the nondimensional load and displacement at the center of the plate by $p^* = p_0 \, a^4/E_1 \, h^4$ and $W^* = w_c/h$, respectively, in Figure 5 are represented the load-displacement paths obtained with the present model (PM), and those obtained by Nath and Kumar [3], where a very good agreement is observed.

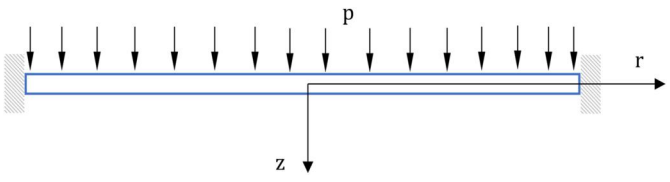

Figure 4. Composite clamped circular plate subjected to uniform pressure.

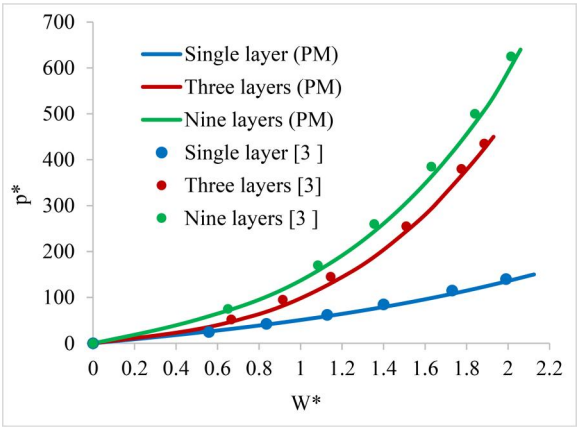

Figure 5. Effect of the number of layers on deflections of a clamped circular plate.

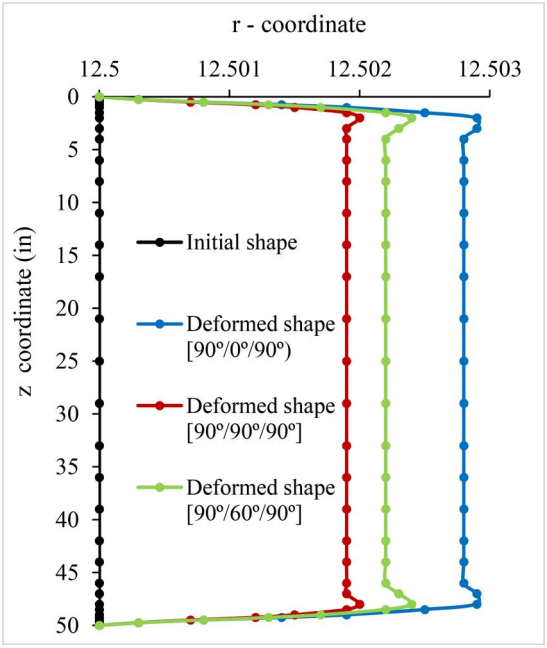

Figure 6. Deformed shape.

5.2. Linear analysis of a clamped laminated cylinder under internal uniform pressure

A three-layered composite cylinder, clamped at both ends is subjected to an internal uniform pressure. The fiber orientation is [90°/α/90°] measured from the meridional direction. The geometry is defined by the radius $R=12.5$ in, the length $L=50.0$ in, and the thickness $h=0.25$ in. The material is Boron-Epoxy with the following material data: $E_1=32.5\times10^6$ psi, $E_2=1.84\times10^6$ psi, $G_{12}= G_{13} = 0.642\times10^6$ psi, $\nu_{12} = 0.256$. Considering the uniform pressure load $q_0=100.0$ psi, the deformed shape for the lamination sequence [90°/α°/90°] is shown in Figure 6. In Figures 7 and 8(a), the deformed shape and circumferential stresses, $\sigma_\theta = \sigma^m_\theta + \sigma^b_\theta$, respectively, obtained with present model (PM) are validated with an alternative solution obtained with Abaqus [14] quadrangular shell finite element model, S4R and the degenerated triangle S3 model, by using a mesh of 7140 elements resulting in a problem with 131,040

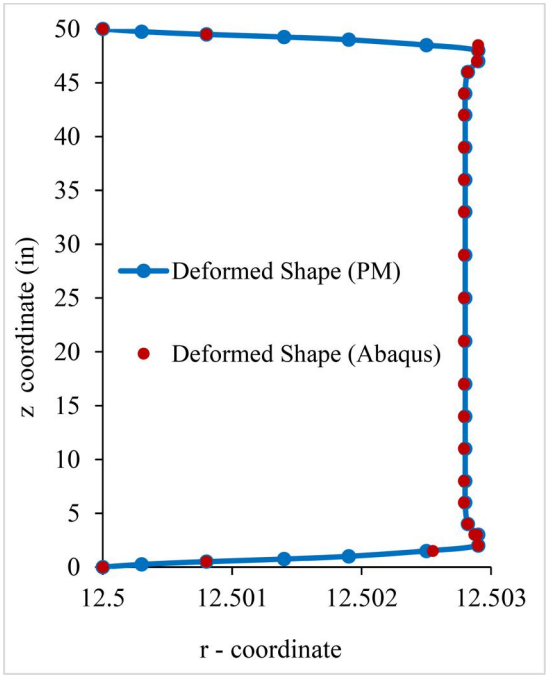

Figure 7. Deformed shape for [90°/0°/90°] validated with an alternative solution.

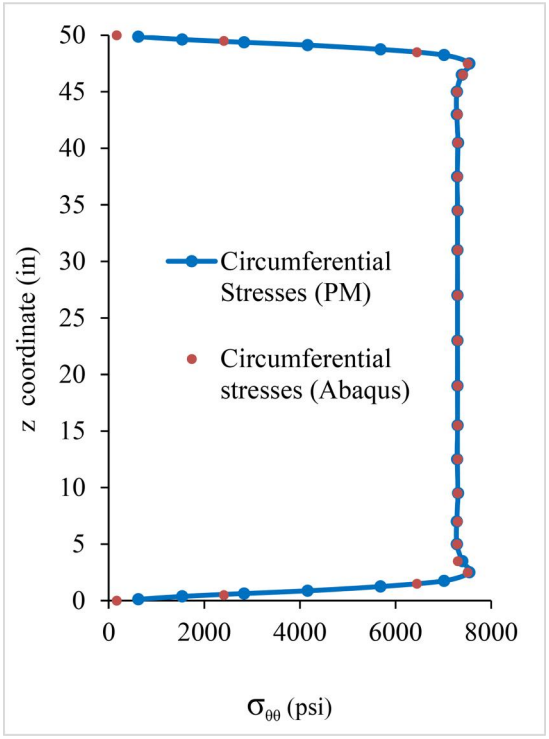

Figure 8. Circumferential stresses validated with an alternative solution.

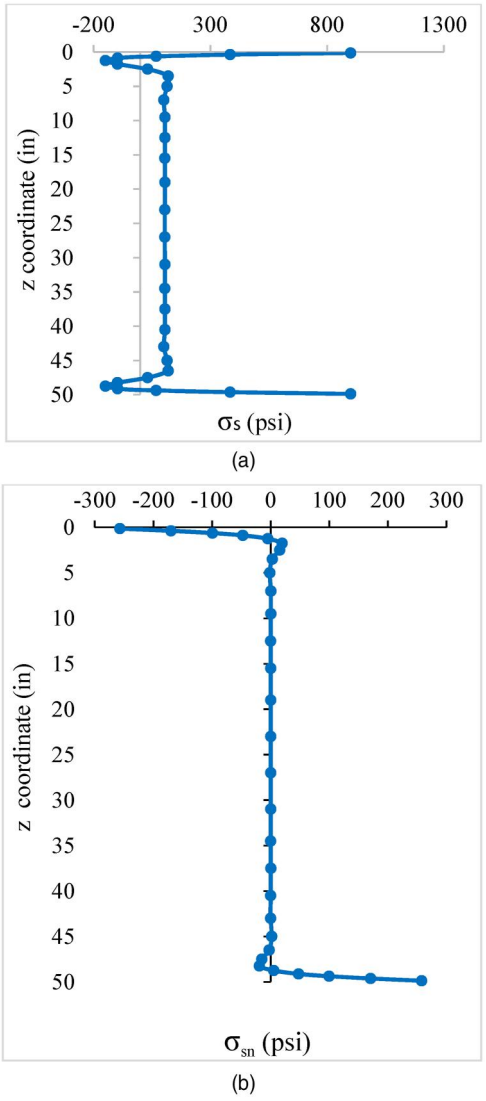

Figure 9. a. Meridional stresses. b. Transverse shear stress.

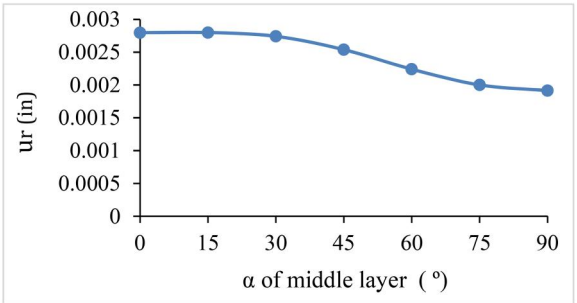

Figure 10. Effect of fiber angle of the middle layer on the centre deflection.

equations. The meridional stresses are shown in Figure 9(a) and the transverse shear stresses σ_{sz}, along any meridian, are shown in Figure 9(b).

Next, the effect of the fiber angle of the middle layer on the deflections of the cylinder is analyzed. The results are shown in Figure 10, where it can be observed that the angle of 90° leads to the lowest deflection.

If we consider the same clamped cylinder, but fabricated with three composite layers with the lay-up [30°/0°/−60°], and the layer thicknesses of $h_1=h_2=h_3=0.083334$ in, representing a non-symmetric lay-up, we need to consider the symmetric and anti-symmetric parts of the displacement vector. By using a number of harmonics, nh = 0, Figure 11(a) shows the radial displacements for the composite [30°/0°/−60°] cylinder, considering coupling and no-coupling, where it can be observed that both curves are coincident. The anti-symmetric displacements are not captured with

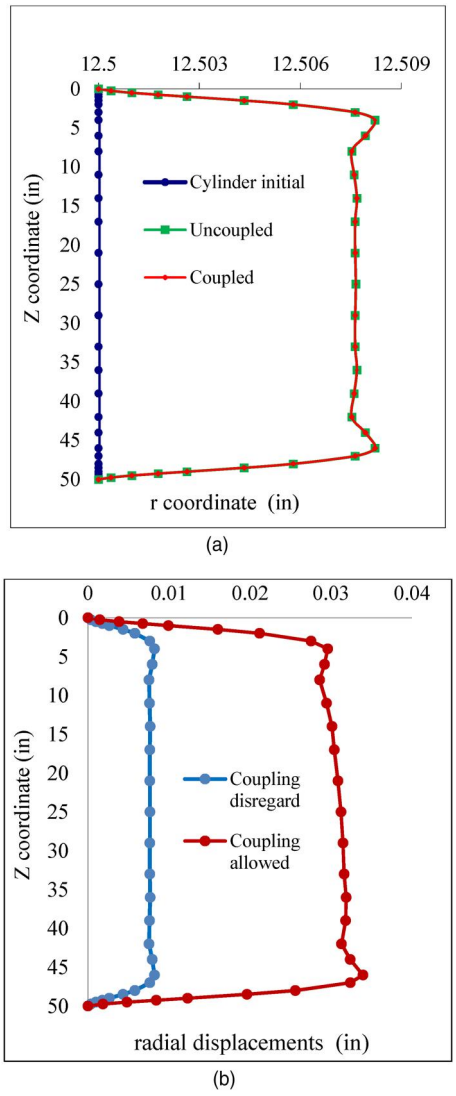

Figure 11. a. Radial displacements for composite [30°/0°/−60°] cylinder, considering nh = 0. b. Radial displacements for composite [30°/0°/−60°] cylinder, considering nh = 4.

nh = 0. In this case, we must use nh > 0. In Figure 11(b), the displacement curves obtained using nh = 4, comparing the effect of coupling considered and no-coupling or coupling disregarded. It can be observed that when coupling is considered, a more flexible structure is obtained.

5.3. Nonlinear analyses of a hybrid spherical cap

A hybrid composite having lower and upper FGM skins (F/C/F), spherical cap, with the geometry represented in Figure 12, is now addressed. The cap has a curvature radius of $R = 2.286$ m, half-opening angle $\phi_0 = 35°$ and a total thickness of $h = 0.04$ m. The thickness of the four-layered composite material is $4\times h_{C_k} = 0.005$ m, $k = 1,2,34$. The FGM is made of Zirconia (c) and Aluminum (m), with the following material data for ceramic and metal: E_c=151.0 GPa, E_m = 70.0 GPa, ν_c = 0.3, ν_m = 0.3. The material data for the composite layers are: E_{11}=413.71 GPa, E_{22} =10.343 GPa,

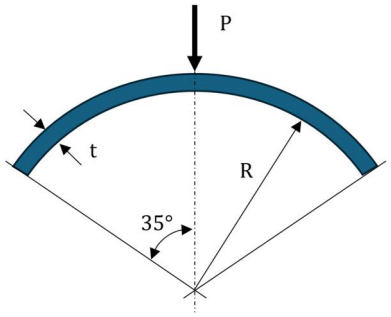

Figure 12. Clamped spherical cap.

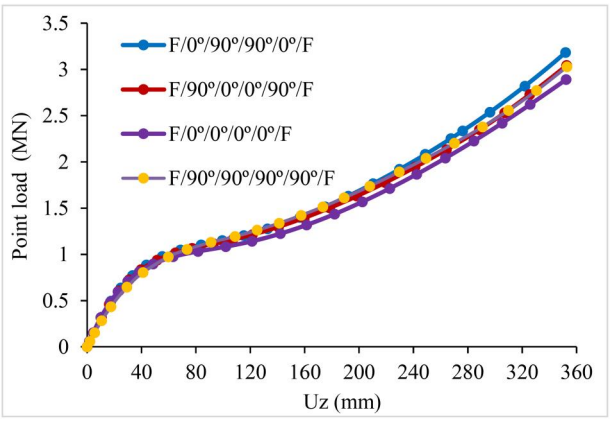

Figure 13. Load–displacement paths for spherical cap.

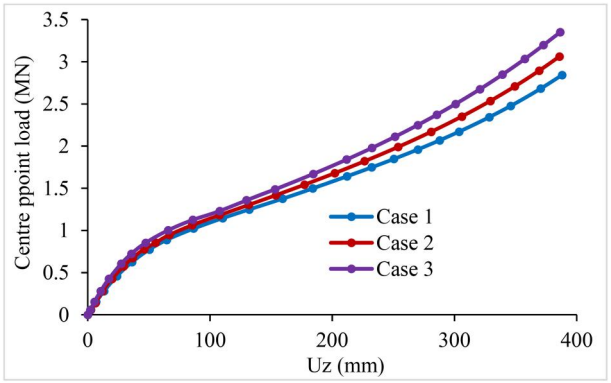

Figure 14. Load–displacement paths for different h_F/h_C and lay-up [F/90°/90°/90°/90°/F].

G_{66}=G_{44}=G_{55}= 6.206 GPa and ν_{12}=0.28. Four different lay-ups are considered, [F/0°/90°/90°/0°/F], [F/90°/0°/0°/90°/F], [F/0°/0°/0°/0°/F] and [F/90°/90°/90°/90°/F], and the gradient index $p = 1.0$ is used. The nonlinear responses of the spherical caps under a central point load are shown in Figure 13. It is observed that the stiffer cap has the lay-up [F/0°/90°/90°/0°/F].

For lay-up [F/90°/90°/90°/90°/F], three different cases of h_F/h_C ratios are considered: case 1, h_F = 0.0075 m and h_C = 0.025 m; case 2, h_F = 0.01 m and h_C = 0.02 m; case 3, h_F = 0.015 m and h_C = 0.01 m. In Figure 14, the load displacement paths for these cases are shown, where it can be observed that case 3 corresponds to the stiffer spherical cap.

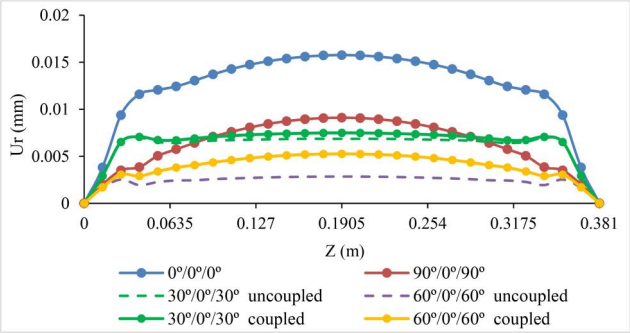

Figure 15. Radial deflections versus axial coordinate for composite [α/0°/α] cylinder.

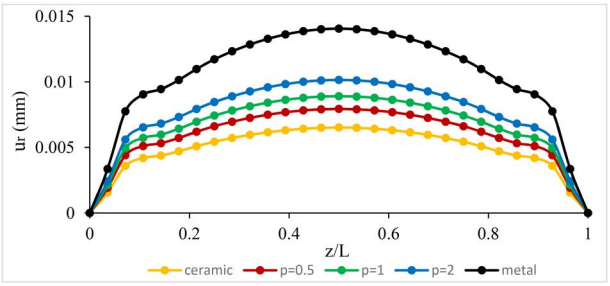

Figure 16. Radial deflections versus axial coordinate for FGM cylinder.

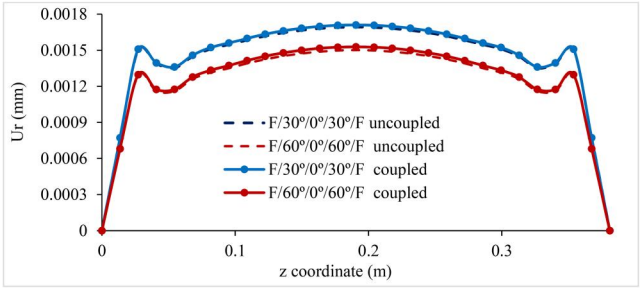

Figure 17. Radial deflections versus axial coordinate for a hybrid cylinder.

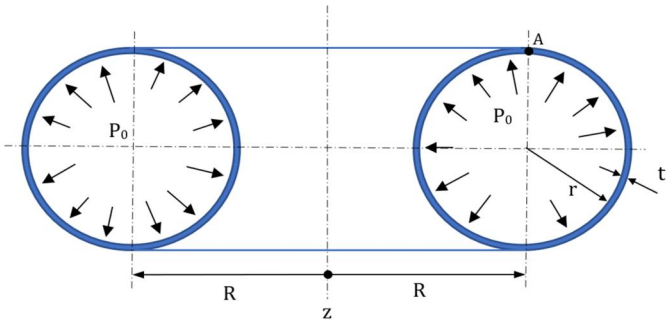

Figure 18. Toroidal shell.

5.4. Clamped laminated cylindrical shell subjected to hydrostatic pressure

A numerical application consisting of a horizontal cylindrical shell, with both edges clamped, having a composite laminate sequence [α/0°/α] is now considered. The material and geometric data are the following: $E_1 = 206.9$ GPa, $E_2 = 18.62$ GPa, $G_{12} = G_{13} = G_{23} = 4.48$ GPa and $\nu_{12} = \nu_{13} = \nu_{23} = 0.28$, $R = 0.1905$ m (radius), $L = 0.381$ m (length) $h = 0.000501$ m. A finite element mesh with 28 elements was used. The cylindrical shell is under an internal surface load $p(\theta) = -p_0(1 + \cos\theta)$ with $p_0 = 1000$ Pa. Figure 15 shows the radial displacements with respect to the Z coordinate. The computed values are obtained considering coupling and for the uncoupled condition, so it becomes visible the influence of the coupling terms, leading to more flexible behavior. Also, it is observed a great coincidence of results with those obtained by Pinto Correia et al. [6] and Santos et al. [7] in both cases by using more sophisticated finite element formulations. Next, the case of an FGM cylinder filled of water, with $p(\theta) = -\rho\ g\ R\ (1 + \cos\theta)$. The water density and acceleration of gravity are respectively ρ and g. The constituents are Zirconia and Aluminum, and the geometry is defined by $R = 0.3$ m, $L = 1$ m, and $h = 5$ mm. The results obtained are shown in Figure 16.

5.5. Clamped hybrid cylindrical shell subjected to hydrostatic pressure

A hybrid horizontal cylindrical shell, with both edges clamped, and lay-up [F/α/0°/α/F] is now analyzed. The material and geometric properties are: $E_1 = 206.9$ GPa, $E_2 = 18.62$ GPa, $G_{12} = G_{13} = G_{23} = 4.48$ GPa and $\nu_{12} = \nu_{13} = \nu_{23} = 0.28$, radius $R = 0.1905$ m, length $L = 0.381$ m total thickness $H = 0.00049$ m. The thickness of each functionally graded layer is $h_F = 0.000125$ m, and the thickness of each of the 3 layers of composite material is $h_{C_k} = 0.00008$ m. The constituents of the FGM layers are the Zirconia and Aluminum with the following material properties $E_c = 380.0$ GPa, $E_m = 70.0$ GPa, $\nu_c = 0.3$, $\nu_m = 0.3$ for the ceramic and the metal, respectively. The gradient index is $p = 1.0$.

The present model uses a finite element mesh with 28 elements. The cylindrical shell is under an internal surface load $p(\theta) = -p_0(1 + \cos\theta)$ with $p_0 = 1000$ Pa. Figure 17 shows the radial displacements along the length. The computed values are obtained considering the coupling and coupling disregarded, by imposing $B = 0$. The radial displacements, in this case, unlike the example in section 5.4, are almost coincident, which is due to the stiffness dominance of the FGM skins, making the terms of sub-matrix B of the constitutive matrix almost zero, $B \sim 0$.

5.6. Analysis of a hybrid toroidal shell, subjected to an internal pressure

The last numerical application consists in a hybrid toroidal shell as shown in Figure 18. The geometry is defined by $r = 254$ mm, $R = 381$ mm and thickness $t = 12.7$ mm. The thickness of the FGM and the composite layers are, respectively: $h_F = 0.00405$ m; $4 \times h_C = 0.00115$ m. The constituents of the FGM layers are the Zirconia, for ceramic (c) and Aluminum, for metal (m), having the following materials data: $E_c = 151.0$ GPa, $E_m = 70.0$ GPa, $\nu_c = 0.3$, $\nu_m = 0.3$. The material data for the composite layers are: $E_{11} = 224.079$ GPa, $E_{22} = 12.687$ GPa, $G_{66} = G_{44} = G_{55} = 4.426$ GPa and $\nu_{12} = 0.256$.

The hybrid toroidal shell is subjected to an interior radial pressure load as schematically represented in Figure 18. The circular section is modeled by using 24 elements and 24

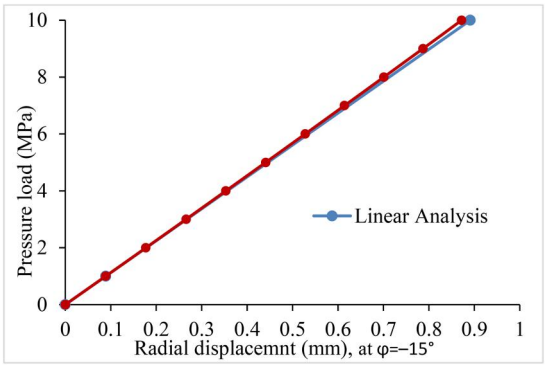

Figure 19. Load–displacement path for the hybrid toroidal shell.

Table 1. Radial displacements at $\phi = -15°$ for different lay-up and gradient index $p = 1$.

Lay-up	Radial displacement (mm)
F/0°/90°/90°/0°/F	0.872
F/90°/0°/0°/90°/F	0.874
F/0°/0°/0°/0°/F	0.408
F/90°/90°/90°/90°/F	1.542
F/F	0.903
0°/90°/90°/0°	0.860

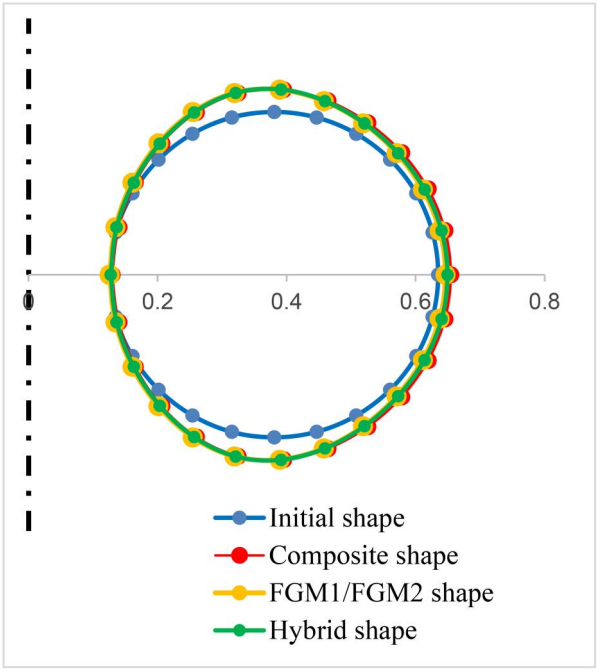

Figure 20. Initial and deformed shapes of a hybrid toroidal shell for index $p = 1.0$.

nodal nodes. Both linear and nonlinear analyses are performed, and the results for the displacement w (see Eq. (4a)), at ϕ=–15°, are shown in Figure 19, for the lay-up [F/0°/90°/90°/0°/F] and the gradient index $p = 1$. The angle ϕ is measured clockwise from point A. The radial displacement as a function of the lay-up, for ϕ=–15°, is given in Table 1. In this table, it is shown the influence of fiber angles and the stiffer structure corresponds to the lay-up [F/0°/0°/0°/0°/F].

The initial and the deformed shapes for FGM and hybrid toroidal shells are shown in Figure 20. In Figure 21, for hybrid shell, are shown the total meridional and

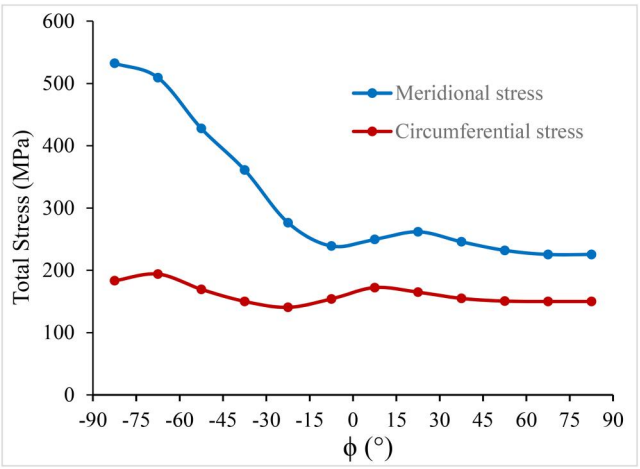

Figure 21. Meridional and circumferential total stresses in the inner layer of the toroidal shell.

circumferential stresses at the inner layer, for the load level q_0=10 MPa. From this figure, it is observed that the meridional stresses are maximum at the inner circle and minimum at the outer circle. On other hand, the circumferential stresses have little change.

6. Conclusions

A finite element model for the static analysis of hybrid axisymmetric shells structures under axisymmetric and non-axisymmetric loads is presented. The static study includes the linear and geometrically nonlinear analyses subjected to mechanical loading. The model used the first order shear deformation theory, and it is based on separating the variables in Fourier series in the circumferential direction with a very simple conical frustum finite element in the meridional direction, which have two nodes and 5 or 10 degrees of freedom per node, depending on the analysis to be performed: 5 for the uncoupled case and 10 for the coupled case. From the presented numerical examples, it is important to note that the geometric nonlinear analysis does not play an important role, unless for the case of the spherical cap: the solutions when large displacements are accounted – nonlinear analysis solutions are very similar to the solutions obtained in linear analysis.

The influence of variation of the gradient index of FGM layers and the fiber angles of composite layers on static displacements was analyzed. Also, the coupling between symmetric and antissymmetric displacement amplitudes has been analyzed. An important conclusion is about the existence of coupling in the presence of composite laminates with nonsymmetric lay-up and functionally graded materials, or whenever there is a nonsymmetric loading.

The present model is very simple, and as shown with the suitable set of numerical applications presented in this work, a very good accuracy is found as the results obtained with the present model compare very well with the alternative solutions available. Those characteristics made it a good numerical model to integrate a multi-objective optimization tool dedicated to axisymmetric structures made of composite and functionally graded materials.

Acknowledgements

The authors dedicate this paper to Professor J. N. Reddy on his 80th birthday for his professional contributions and his impact on research and education in mechanics of advanced composites materials and structures and computational methods, and for is friendship and support over the years to the IDMEC group. The first and fourth coauthors are friends of JN for more than 50 years. Professor Reddy, affectionately known among his friends as "JN", has been a friend of the authors and influenced their professional careers through research collaboration. For his collaboration and guidance of young researchers, he received Doctor Honoris Causa Award from Instituto Superior Técnico, Universidade de Lisboa, Portugal. JN is a scholar, a passionate teacher, a great human being, and an unconditional friend of his friends, students, colleagues, and collaborators with a broad view and horizons of the world that transcend his technical expertise.

Disclosure statement

No potential conflict of interest was reported by the authors.

Funding

The authors acknowledge Fundação para a Ciência e a Tecnologia (FCT) for its financial support via the project LAETA Base Funding (DOI:10.54499/UIDB/50022/2020).

ORCID

Carlos A. Mota Soares http://orcid.org/0000-0003-2628-9829
José S. Moita http://orcid.org/0000-0003-2529-583X
Aurélio L. Araujo http://orcid.org/0000-0003-3994-2516
Victor Franco Correia http://orcid.org/0000-0002-5159-5361
Cristóvão M. Mota Soares http://orcid.org/0000-0002-4645-138X

References

[1] I. Sheinman, and S. Greif, Dynamic analysis of laminated shells of revolution, J. Compos. Mater., vol. 18, no. 3, pp. 200–215, 1984. DOI: 10.1177/002199838401800301.
[2] I. Sheinman, and S. Weissman, Coupling between symmetric and antisymmetric modes in shells of revolution, J. Compos. Mater., vol. 21, no. 11, pp. 988–1007, 1987. DOI: 10.1177/002199838702101101.
[3] Y. Nath, and S. Kumar, Large amplitude response of layered circular plates, J. Eng. Mech., vol. 121, no. 1, pp. 37–49, 1995. DOI: 10.1061/(ASCE)0733-9399(1995)121:1(37).
[4] K. Sandeep, and Y. Nath, Nonlinear analysis of unsymmetrically laminated moderately thick axisymmetric structures, Int. J. Nonlin. Sci. Numer. Simulat., vol. 1, no. 3, pp. 215–223, 2000. DOI: 10.1515/IJNSNS.2000.1.3.215.
[5] C.M. Mota Soares, N.M. Cordeiro, and J.I. Barbosa, A discrete model for the design sensitivity analysis of multi-layered composite shells of revolution, Compos. Eng., vol. 5, no. 5, pp. 533–550, 1995. DOI: 10.1016/0961-9526(95)00027-K.
[6] Pinto Correia I.F., Barbosa J.I., Mota Soares C.M., and Mota Soares C. A., A finite element semi-analytical model for laminated axisymmetric shells: statics, dynamics and buckling, Comput. Struct., vol. 76, no. 1–3, pp. 299–317, 2000. DOI: 10.1016/S0045-7949(99)00165-0.
[7] H. Santos, C.M. Mota Soares, C.A. Mota Soares, and J.N. Reddy, A semi-analytical finite element model for the analysis of laminated 3d axisymmetric shells: bending, free vibration and buckling, Compos. Struct., vol. 71, no. 3–4, pp. 273–281, 2005. DOI: 10.1016/j.compstruct.2005.09.006.
[8] J. Flis, and A. Muc, Influence of coupling effects on analytical solutions of functionally graded (FG) spherical shells of revolution, Rev. Adv. Mater. Sci., vol. 60, no. 1, pp. 761–770, 2021. DOI: 10.1515/rams-2021-0064.
[9] J.S. Moita, A.L. Araujo, V. Franco Correia, and C.M. Mota Soares, Free vibrations analysis of composite and hybrid axisymmetric shells, Compos. Struct., vol. 286, pp. 115267, 2022. DOI: 10.1016/j.compstruct.2022.115267.
[10] O.C. Zienkiewicz, J. Bauer, K. Morgan, and E. Onate, A simple and efficient element for axisymmetric shells, Numer. Meth. Eng., vol. 11, no. 10, pp. 1545–1558, 1977. DOI: 10.1002/nme.1620111006.
[11] J.S. Moita, A.L. Araújo, V. Franco Correia, and C.M. Mota Soares, Mechanical and thermal buckling of functionally graded axisymmetric shells, Compos. Struct., vol. 261, pp. 113318, 2021. DOI: 10.1016/j.compstruct.2020.113318.
[12] A. Arbind, and J.N. Reddy, A one-dimensional model of 3-D structure for large deformation: a general higher-order rod theory, Acta Mech., vol. 229, no. 4, pp. 1803–1831, 2018. DOI: 10.1007/s00707-017-2048-4.
[13] A. Arbind, J.N. Reddy, and A.R. Srinivasa, A nonlinear 1-D finite element analysis of rods/tubes made of incompressible neo-Hookean materials using higher-order theory, Int. J. Solids Struct., vol. 166, pp. 1–21, 2019. DOI: 10.1016/j.ijsolstr.2019.01.023.
[14] ABAQUS/Standard User's Manual, Dassault Systems Simulia Group, 2009.

Appendix. Developed program schematics